

Enhanced Weather Surveillance Capabilities With Multiple Simultaneous Transmit Beams

David Schwartzman^{ID}, Senior Member, IEEE, Robert D. Palmer^{ID}, Fellow, IEEE,
Matthew Herndon^{ID}, Member, IEEE, and Mark B. Yeary^{ID}, Fellow, IEEE

Abstract—Phased array radar (PAR) represents the future of polarimetric weather surveillance, driven by the need for high-temporal resolution observations to improve storm monitoring and precipitation analysis. This study presents a novel technique for generating multiple simultaneous transmit beams using phase-only beamforming weights. Unlike previous methods, this approach generates multiple narrow and separate transmit peaks, minimizing sensitivity loss (compared to broadened beams) and improving sidelobe isolation. Bézier surfaces are used to parametrize the element-level phases across the array, producing a smooth distribution with reduced optimization complexity. This article outlines the theoretical formulation, demonstrates simulation results of the phase-only optimization, and validates the method with experimental data collected with the fully digital Horus PAR. Validation using a point target revealed precise beam pointing with angular accuracy within 0.1°, and measurements during a severe weather event resulted in high-quality polarimetric measurements. Scatterplots comparing the Horus radar data to that from the KCRI [Weather Surveillance Radar—1988 Doppler (WSR-88D)] radar show high correlations (e.g., reflectivity correlation coefficient of 0.91), underscoring the accuracy and reliability of the approach. These findings highlight the potential of multiple simultaneous beams for the next-generation weather radar systems, enabling high-temporal resolution observations and advanced capabilities for weather surveillance.

Index Terms—Antenna pattern synthesis, digital beamforming (DBF), digital phased array radar (PAR), polarimetric radar, weather radar.

I. INTRODUCTION

HIGH-TEMPORAL resolution polarimetric radar observations are essential for deepening our understanding of atmospheric processes and enhancing weather surveillance capabilities. Polarimetric radars, which transmit and receive signals in both horizontal (H) and vertical (V) polarizations,

Received 5 August 2024; revised 11 November 2024 and 31 December 2024; accepted 7 January 2025. Date of publication 9 January 2025; date of current version 29 January 2025. This work was supported by the National Oceanic and Atmospheric Administration (NOAA) /Office of Oceanic and Atmospheric Research through NOAA-University of Oklahoma Cooperative Agreement under Grant NA21OAR4320204, U.S. Department of Commerce. (*Corresponding author: David Schwartzman*)

David Schwartzman is with the Advanced Radar Research Center (ARRC), the School of Meteorology, and the School of Electrical and Computer Engineering, The University of Oklahoma, Norman, OK 73019 USA (e-mail: dschvart@ou.edu).

Robert D. Palmer is with the Advanced Radar Research Center (ARRC) and the School of Meteorology, The University of Oklahoma, Norman, OK 73019 USA.

Matthew Herndon and Mark B. Yeary are with the Advanced Radar Research Center (ARRC) and the School of Electrical and Computer Engineering, The University of Oklahoma, Norman, OK 73019 USA.

Digital Object Identifier 10.1109/TRS.2025.3527882

measure polarimetric variables such as differential reflectivity (Z_{DR}), differential phase (Φ_{DP}), and copolar correlation coefficient (ρ_{hv}), which are critical for identifying hydrometeor types (e.g., rain, snow, and hail) and improving quantitative precipitation estimates [1]. Timely, high-quality polarimetric weather information can mitigate the impacts of severe weather events by enabling early warnings and providing insights into storm dynamics [2]. For instance, high-temporal resolution data from weather radars can help meteorologists identify and track severe weather phenomena, allowing authorities to issue prompt warnings and reduce potential casualties and property damage. Moreover, these observations improve numerical weather prediction models, which rely on high-quality data for accurate forecasts [3].

Phased array radar (PAR) technology, which enables faster volume update times and flexible scanning strategies, has emerged as a leading candidate for the next generation of weather radars [3], [4], [5]. Unlike traditional parabolic dish radars, PAR systems can electronically steer beams to capture rapidly evolving storm structures with high-temporal resolution. This capability is particularly crucial for observing rapidly developing weather phenomena such as severe thunderstorms, hail, and tornadoes, where the ability to capture high-temporal resolution data can lead to better understanding and prediction of these events. Studies have shown the benefits of PAR in meteorology, highlighting its ability to provide detailed storm observations and improve warning decision-making by providing data with higher temporal resolution [6], [7], [8]. Heinselman et al. [6] demonstrated PAR's utility in visualizing rapidly changing storm features, while Bowden et al. [7] found that higher temporal updates helped forecasters make faster, more accurate warnings. In 2017, Kurdzo et al. [10] investigated the benefits of using the atmospheric imaging radar (AIR), which used an intentionally broadened or “spoiled” transmit beam, for observing severe weather phenomena [9]. The AIR’s rapid scanning capabilities allowed for detailed analysis of storm dynamics and rapid evolution, offering significant advantages over traditional radar systems especially when observing severe and potentially tornadic storms. Mizutani et al. [11] demonstrated a PAR with fast scanning and wide elevation coverage, also using a spoiled transmit beam, allowing simultaneous observations at multiple elevation angles. This system achieved high temporal and spatial resolution, enabling the early detection of severe weather phenomena such as precipitation cores, which

were detected minutes before reaching the ground, thereby improving warning capabilities and potentially mitigating weather-related damages.

Intentionally broadened or “spoiled” transmit beams are designed to have a wider mainlobe, allowing for a larger area to be illuminated during each transmission [9], [12]. On reception, digital beamforming (DBF) is used to simultaneously form multiple receive beams within the broad transmit illumination. A conceptual illustration of a spoiled beam is shown in Fig. 1(a) (from [10]). This enables high-temporal resolution observations although challenges associated with their use in radar meteorology must be considered. These include degraded angular resolution, increased sidelobe levels, and reduced sensitivity compared to narrow pencil beams achievable with the same aperture. The increased sidelobe levels are a direct consequence of distributing the beam’s power more evenly across a wider area on transmission, which reduces the directivity of the two-way beams (i.e., the product of the transmit and receive antenna patterns). The degradation in sidelobe performance can contaminate the received signal with unwanted echoes, ultimately compromising the quality of polarimetric measurements and the accuracy of meteorological observations. These tradeoffs must be carefully considered in the design of advanced scanning strategies to meet operational requirements [13], [14], [15].

A more suitable mode of operation for achieving low two-way sidelobe levels in PAR systems is the use of a beam with multiple simultaneous transmit beams, as shown in Fig. 1(b). This approach involves synthesizing transmit beams with multiple separate peaks, which can illuminate different regions of the atmosphere simultaneously. By doing so, it is possible to improve the temporal resolution of weather observations without increasing the beamwidth or the two-way sidelobe levels [16]. The ability to generate multiple simultaneous beams is particularly advantageous for polarimetric weather radars, where maintaining high data quality is critical [17]. In contrast with spoiled transmit beams, the use of multiple simultaneous beams provides a more effective solution, maintaining narrow and well-defined transmit beams in different directions. As a result, the two-way pattern—the combined effect of the transmit and receive patterns—exhibits superior performance in terms of sidelobe isolation and angular resolution. In fact, the receive beams can be designed to have nulls in the directions of the other transmit peaks greatly improving two-way sidelobe performance. This is critical for high-resolution and high-quality polarimetric measurements, as it minimizes the contamination from sidelobe returns and enhances the radar’s ability to distinguish between different types of precipitation. The main tradeoff when using this mode is that there is an inevitable reduction in gain, proportional to the number of beams synthesized. That is, if three beams are synthesized, the gain of each transmit peak is about one-third of what would be achieved using a full aperture pencil beam.

To synthesize multiple simultaneous beams, an optimization algorithm that produces phase-only weights to excite the phased array antenna is proposed. Phase-only beamforming is preferred because it avoids the power losses associated with amplitude tapering and ensures that the maximum possible

transmit gain is achieved. The optimization process involves shaping the antenna pattern and controlling the sidelobe levels to meet specific design criteria, essential for accurate weather observations [12]. Our approach leverages a hybrid optimization method that combines a measured antenna element pattern with a pattern synthesis optimization to find a set of phase weights that synthesize the desired beam. Given the relatively large number of antenna elements, each associated with a variable phase coefficient, a phase parametrization function is used to reduce the number of variables in the search space.

While previous work has explored methods for generating multiple beams with PAR, our approach introduces significant advancements in both the algorithm and its practical implementation. Yoshikawa et al. [18] introduced a method for generating “comb beams” through a deterministic approach that utilizes both amplitude and phase weights. While effective in generating multiple beam peaks, this method incurs sensitivity losses due to amplitude tapering, which reduces the overall transmit power. For high-sensitivity applications like weather radar, maintaining maximum transmit power is essential for capturing weak meteorological signals. In contrast, our proposed approach generates multiple simultaneous beams through *phase-only* beamforming, which achieves higher transmit gain by avoiding amplitude tapering. Additionally, Yoshikawa et al. [18] demonstrated their method only through numerical simulations, whereas this study implements and validates this phase-only approach on an operational radar system, including polarimetric weather measurements collected during a severe weather event. Furthermore, our method achieves beam patterns with 2-D beam-pointing offsets (azimuth and elevation), enhancing sidelobe isolation beyond the 1-D approach demonstrated by Yoshikawa et al. [18].

The primary contributions of this article are as follows: 1) development and implementation of a phase-only beamforming algorithm to generate multiple simultaneous transmit beams, maximizing system sensitivity; 2) enabling the synthesis of multiple beams steered in both azimuth and elevation; and 3) validating this method with a fully digital PAR to achieve high-quality polarimetric weather measurements. This article is structured as follows. Section II covers the theoretical foundations of the multiple simultaneous beams concept and the optimization algorithm for beam synthesis. Section III presents the results from beams synthesized using the proposed optimization method. Section IV provides an experimental demonstration of the synthesized antenna patterns on the Horus radar, showcasing weather data collection and evaluating polarimetric variable quality. Results confirm the radar’s ability to collect high-resolution, high-quality polarimetric data, essential for the next-generation weather radar systems, using the proposed beamforming mode. Finally, Section V concludes with a summary of findings and directions for future research.

II. THEORETICAL FORMULATION

Phase-only pattern synthesis is a complex optimization problem, often involving the use of iterative algorithms to find a set of phase weights that meet prescribed sidelobe levels while maintaining a mainlobe of specific width. The challenge

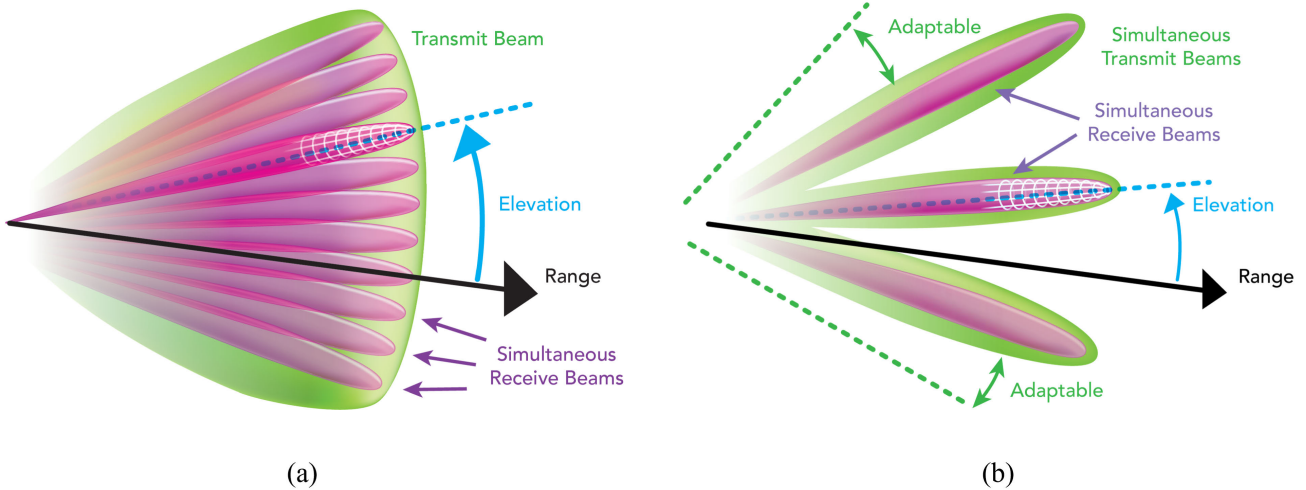


Fig. 1. (a) Spoiled transmit beam, adapted from [10]. (b) Beam with multiple simultaneous transmit peaks in different directions.

is to achieve the desired performance (i.e., beam shape and sidelobe levels) with phase adjustments alone, which can be less flexible than using amplitude and phase control. Despite these challenges, significant strides have been made in this area to synthesize phase-only beam patterns with different shapes [19], [20].

Given the relatively large number of antenna elements that would need to be optimized for PARs, phase weights are parametrized to reduce the number of variables in the search space. That is, a parametric function is used to represent the phase excitation of a group of antenna elements; thus, only the parameters defining the function need to be optimized. Previous research efforts have shown that Bézier surfaces and nonuniform rational B-splines (NURBS) can be used as the parametric functions [21], [22]. In this article, we use Bézier surfaces, the generalization of a Bézier curve, defined by a set of control points in which this smooth curve passes through the first and last control points. Next, we provide a mathematical background for the proposed synthesis method using Bézier curves to parametrize the complex phase weights.

A. Antenna Pattern Model

The array factor of a planar PAR is modeled as follows:

$$\text{AF}(\theta, \phi) = \sum_{m=1}^M \sum_{n=1}^N w_{mn} e^{-j(m\Psi_x + n\Psi_y)} \quad (1)$$

where w_{mn} is a complex weight (magnitude and phase) for the element in the m th row and n th column, $\Psi_x = kd_x \sin(\theta) \cos(\phi)$, $\Psi_y = kd_y \sin(\theta) \sin(\phi)$, $k = (2\pi/\lambda)$ is the wavenumber, λ is the wavelength, θ and ϕ are the azimuth and elevation angles, respectively, and d_x and d_y are the element spacings in the x - and y -directions, respectively. Herein, we assume that $d_x = d_y = (\lambda/2)$.

We are interested in searching for phase values to compute the complex weights (w_{mn}) that synthesize different transmit patterns. The array pattern can be approximated using the embedded element patterns and the array factor as

$$F^{pq}(\theta, \phi) = F_e^{pq}(\theta, \phi) |\text{AF}(\theta, \phi)|^2 \quad (2)$$

where $F_e^{pq}(\theta, \phi)$ represents the embedded element pattern, and p and q could be either "h" or "v" for the horizontal or vertical polarizations.

B. Fully Digital Horus PAR

The Horus radar shown in Fig. 2, developed by The University of Oklahoma's Advanced Radar Research Center (ARRC), Norman, OK, USA, is a state-of-the-art fully digital, polarimetric S-band PAR designed for the next-generation weather surveillance. Unlike most other PARs, Horus features a fully digital architecture, where each antenna element has an independent digital transmitter and digital receiver per element per polarization, allowing for unparalleled flexibility in calibration, beamforming, and data acquisition [23]. This digital design enables advanced array scanning and processing techniques that can significantly enhance the radar's performance in various weather observation scenarios. Utilizing Analog Devices AD9371 digital transceivers and field-programmable gate array (FPGA)-based signal processing, the Horus radar can compute multiple simultaneous receive beams, to improve temporal resolution and sampling of meteorological observations. The system is liquid-cooled and mounted on a mobile truck platform with a 150-kW power generator, ensuring stable operation and easy field deployment. Designed for high-quality polarimetric measurements, Horus achieves polarimetric calibration using an in situ mutual-coupling calibration algorithm [24], [25]. Polarimetric calibration of weather radars is crucial for accurate precipitation estimation, for understanding microphysical processes, and for hydrometeor classification [26]. The Horus technology represents a significant leap forward in weather observation technology.

The Horus embedded element patterns shown in Fig. 3 were derived from measurements and are used here to model the full Horus array pattern. Note that these are presented in the Ludwig-II coordinate system (Earth-relative azimuth/elevation angles). These measurements serve as a basis for full array patterns to be calculated.



Fig. 2. Horus system, a mobile, fully digital, S-band polarimetric phased array weather radar [23].

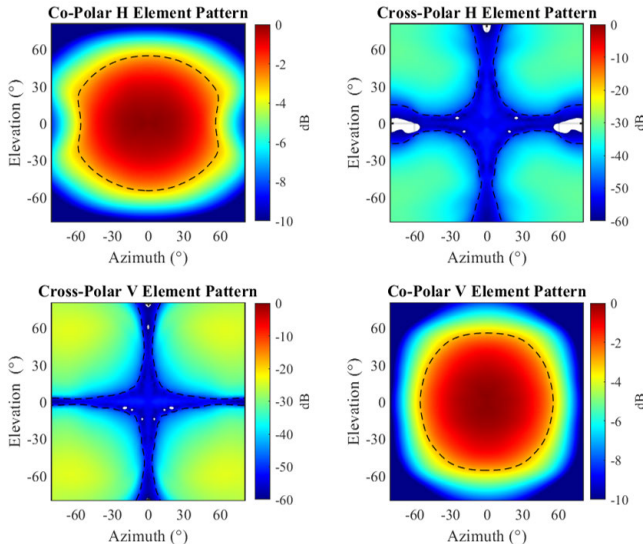


Fig. 3. Measured Horus embedded element patterns. The black dotted contour lines represent the -3 - and -50 -dB levels in the co- and cross-polar patterns.

C. Parameterization With Bézier Surfaces

To manage the large number of variables associated with the phase-only antenna pattern synthesis, Bézier surfaces are used to parametrize the phase excitation across the array. The choice of Bézier surfaces is motivated by their ability to provide smooth, continuous phase distributions with a reduced number of variables, which simplifies the optimization process. Bézier surfaces offer computational efficiency by requiring fewer control points to represent the phase shifts across the array. While effective for most applications, Bézier surfaces may face limitations with highly nonlinear phase profiles. In such cases, alternative parameterizations, such as NURBS, may be considered, as they offer enhanced flexibility in complex phase shaping. Furthermore, in this work, we demonstrate the feasibility of using Bézier surfaces for phase-only synthesis. While this approach provides a practical solution, future work could explore the statistical properties of the phase weights derived (e.g., mean and variance) across multiple optimizations to assess uncertainty and robustness of produced phased weights. Such an analysis could lead to refined beamforming weights and offer a broader interpretation of the optimization results.

Bézier surfaces, an extension of Bézier curves into two dimensions, provide a flexible mathematical framework for smoothly controlling the spatial distribution of phase excitations. A Bézier surface is defined by a grid of control points, where each control point influences the shape of the surface. The density of control points affects how finely the phase distribution can be controlled across the array. The higher density of control points allows for finer phase adjustments and potentially more accurate beam patterns but also increases the computational complexity of the optimization. In this article, a balance was chosen to achieve effective beam synthesis while maintaining computational feasibility.

The surface itself is a bilinear interpolation of these control points, governed by Bernstein polynomials in both dimensions. Given a set of control points P_{ij} , where $i \in [0, p]$ and $j \in [0, q]$, the Bézier surface $S(u, v)$ is mathematically expressed as

$$S(u, v) = \sum_{i=0}^p \sum_{j=0}^q P_{ij} B_{i,p}(u) B_{j,q}(v) \quad (3)$$

where $B_{i,p}(u)$ and $B_{j,q}(v)$ are the Bernstein polynomials of degrees p and q in the parameters u and v , respectively, with both $u, v \in [0, 1]$. These polynomials are given by

$$B_{i,p}(u) = \binom{p}{i} u^i (1-u)^{p-i} \quad (4)$$

$$B_{j,q}(v) = \binom{q}{j} v^j (1-v)^{q-j} \quad (5)$$

where $\binom{p}{i}$ is a binomial coefficient calculated as $(p!/(i!(p-i)!))$.

However, not every element in the antenna array is represented by a Bézier surface control point. Instead, the phase weights of the array elements are sampled from the Bézier surfaces, which are controlled by a smaller number of control points. This approach reduces the dimensionality of the optimization problem significantly.

Let ϕ_{mn} represent the phase excitation of the element in row m and column n of the antenna array. The phase excitation can be expressed as a function of the Bézier surface as follows:

$$\phi_{mn} = S\left(\frac{m}{M-1}, \frac{n}{N-1}\right) \quad (6)$$

where M and N are the total number of rows and columns of the antenna array with $m = 1, 2, \dots, M$ and $n = 1, 2, \dots, N$, and

$$w_{mn} = e^{j\phi_{mn}}. \quad (7)$$

By sampling the Bézier surfaces at regular intervals corresponding to the array element locations, phase excitations needed for each element are derived. This parameterization allows for efficient synthesis of the array's phase weights by adjusting the control points P_{ij} . The resulting phase distribution can be finely tuned to achieve the desired radiation pattern, such as intentionally broadened (or spoiled) beams and the beams with multiple simultaneous peaks, while minimizing sidelobe levels and maintaining mainlobe integrity.

Section II-D will detail the optimization process used to adjust these control points to synthesize the desired antenna radiation patterns.

D. Pattern Synthesis Optimization

The optimization of Bézier surface parameters to produce desired phased array patterns involves a complex interplay between the geometry of the control points and the resulting electromagnetic properties of the beam. Computational algorithms, such as gradient descent or evolutionary strategies (e.g., genetic algorithms or particle swarm optimization), can be employed to iteratively adjust the control points, minimizing the difference between the achieved and desired beam patterns. Furthermore, the use of Bézier surfaces introduces an added layer of flexibility in handling the physical constraints and performance criteria inherent to phased array design. For instance, constraints on phase continuity and smoothness across the array can be naturally incorporated into the optimization process, ensuring that the resulting phase excitation patterns are practically feasible for the desired number of simultaneous beams and sidelobe levels. Bézier surfaces are used to parameterize the phases in (1), namely, the phase of the complex w_{mn} weights.

The optimization is posed as follows:

$$\begin{aligned} \min_{\angle w_{mn} \in [-\pi/2, \pi/2]} & 8 \text{ IC} + \text{EL} \\ \text{s.t. } & |w_{mn}| = 1 \end{aligned} \quad (8)$$

where $\angle w_{mn}$ represents the phase of w_{mn} , and the integrated contamination (IC) is the volume of the synthesized pattern that exceeds a predefined pattern design envelope, $E(\theta, \phi)$, defined in dB as

$$\text{IC} = 10 \log_{10} \left[\frac{1}{4\pi} \int_{-\pi/2}^{\pi/2} \int_{-\pi}^{\pi} \frac{\max[F^{\text{hh}}, E]}{E} \sin(\phi) d\theta d\phi \right] \quad (9)$$

where we have omitted the explicit dependence on θ and ϕ in $F^{pq}(\theta, \phi)$ and $E(\theta, \phi)$ to simplify the notation. The envelope function $E(\theta, \phi)$ is designed to achieve a specified mainlobe width and control sidelobe levels, which are essential for maintaining desired angular resolution and limiting sidelobe contamination. To create an effective envelope, it is important to ensure that $E(\theta, \phi)$ aligns with the desired beamwidth, constrains sidelobe levels to reduce contamination (based on application requirements), and maintains a smooth, continuous shape that aids convergence in the optimization process. Irregular or overly complex patterns may hinder convergence or lead to suboptimal beam patterns. Additionally, beam placement should follow the guideline of spacing beams by a spacing of at least twice the half-power beamwidth to prevent mainlobe merging and maintain desired sidelobe levels. The beamwidth, θ_1 , is defined as the angular width in degrees within which the microwave radiation is greater than one-half of its peak intensity, i.e., $10 \log_{10}(0.5) > -3$ dB [27]. The beamwidth is a standard measure in weather radar systems to define angular resolution. Readers are referred to [20] and [28] for further details on general beam pattern synthesis. These considerations provide guidance for adapting this method to various radar system requirements.

For a three-beam configuration, the envelope function $E(\theta, \phi)$ constrains the synthesized beam pattern by defining

desired mainlobe widths, angular spacing, and sidelobe roll-off characteristics. With mainlobe widths θ_M and ϕ_M , and beam spacings $\Delta\theta$ and $\Delta\phi$, $E(\theta, \phi)$ is defined as (10), as shown at the bottom of the next page, where $k \in \{-1, 0, 1\}$ indexes the three beam peaks in azimuth and elevation, α is the slope (in dB/ $^\circ$) within the sidelobe region, and L is a constant low level for the secondary sidelobe regions. This configuration provides effective mainlobe performance and sidelobe control for the synthesis of radiation patterns with three simultaneous beams.

The efficiency loss (EL) is the integrated power ratio (linear units) between the synthesized pattern over θ_1 and a normalized gain value of 1 (0 dB). The EL is expressed in dB as

$$\text{EL} = -10 \log_{10} \left[\frac{1}{4\pi} \iint_{F^{\text{hh}} > 0.5} \min[F^{\text{hh}}, E] \sin(\phi) d\theta d\phi \right]. \quad (11)$$

The weights used for the performance metrics in the cost function in (8), which are 8 for IC and 1 for EL, were derived empirically and put more emphasis on the sidelobe levels than the EL. Examples of $E(\theta, \phi)$ are shown in Fig. 4 for different beam spacings, where the top ones are for beams offset in one dimension and the bottom ones are for beams offset in azimuth and elevation. The tilting of the peaks in the bottom envelopes can be adjusted to match desired elevation angles. If the synthesized antenna pattern is below the predefined envelope, the IC is 0 dB. Similarly, if the antenna pattern gain within the beamwidth is uniformly 1 in linear units (i.e., 0 dB), the EL is 0 dB. This is because the EL is calculated only within the beamwidth (where $F^{\text{hh}} > 0.5$), allowing to assess how closely the synthesized pattern conforms to the design envelope in this critical part of the beam. In (8), the interaction between IC and EL is managed through the assigned weights, as these parameters represent competing aspects of the antenna pattern. Minimizing IC often results in a corresponding increase in EL, and vice versa, with the optimization solver balancing these competing terms based on the chosen weights. This structure allows control over the tradeoff between maximizing pattern gain within the envelope and limiting integrated sidelobe levels exceeding it.

The choice of phase-only optimization preserves the array gain by maintaining constant amplitude across elements, maximizing the total transmitted power—a key requirement for observing relatively weak signals from atmospheric scatterers. Amplitude weighting and phase weighting allow for more refined control over beam shape but reduce the array gain due to amplitude tapering. For distributed volume targets such as precipitation, maintaining high sensitivity is prioritized, and the advantages of phase-only optimization in achieving this goal outweigh the benefits gained by applying amplitude weighting.

III. SYNTHESIZED ANTENNA PATTERNS

In this section, we illustrate the performance of the proposed optimization to synthesize transmit beams with multiple simultaneous peaks using the current Horus array architecture. The array is populated with electronic components that make up

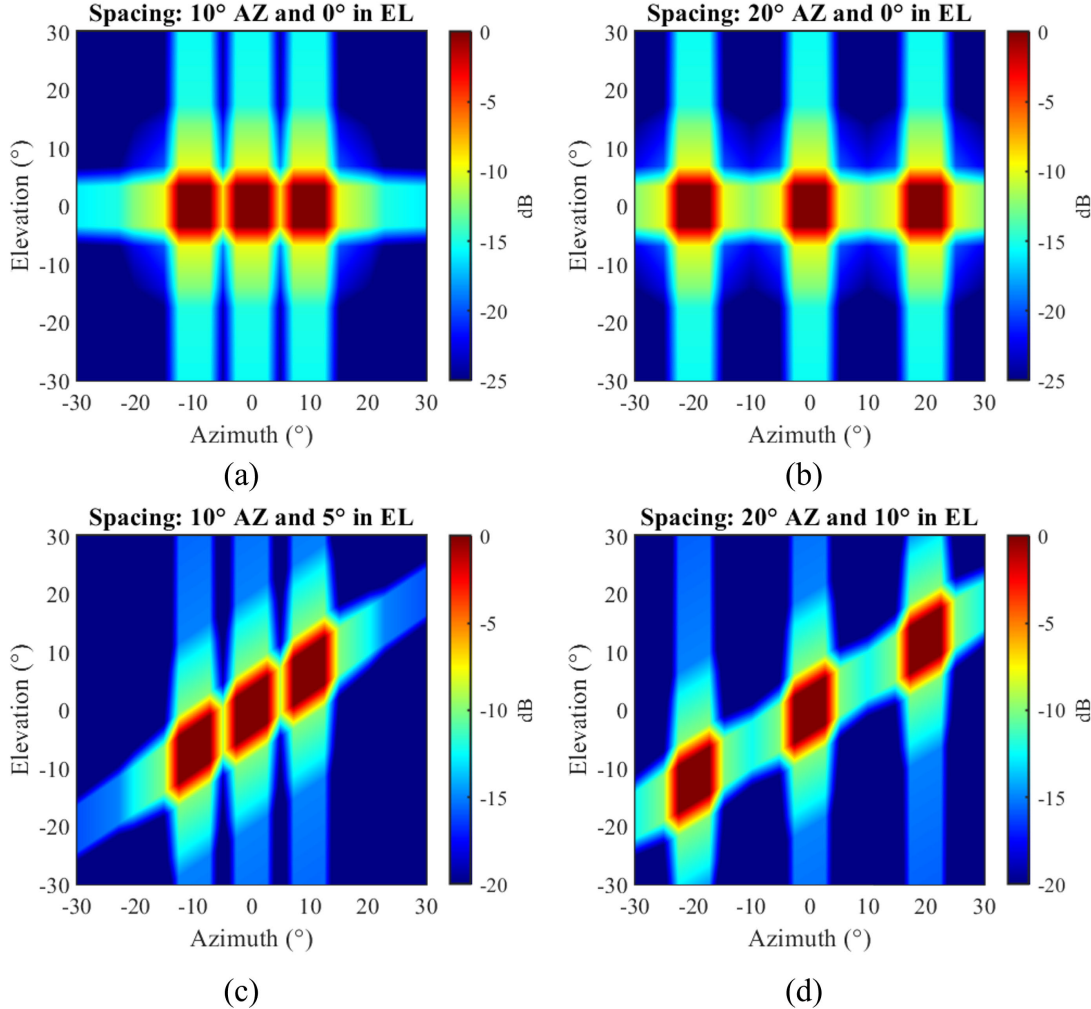


Fig. 4. Antenna pattern design envelopes with spacings of (a) 10° in azimuth and 0° in elevation, (b) 20° in azimuth and 0° in elevation, (c) 10° in azimuth and 5° in elevation, and (d) 20° in azimuth and 10° in elevation.

13 dual-polarization, fully digital array panels (8×8 elements per panel). Panels are arranged in a “diamond-like” configuration, as shown in Fig. 5. The pattern synthesis optimization can produce weights for multiple beams with different angular spacings in azimuth and elevation. The number of simultaneous peaks that can be synthesized and their spacing is a function of the aperture size. Two types of beams will be illustrated: all peaks are aligned in either azimuth or elevation (1-D beamforming), and peaks are offset in both azimuth and elevation (2-D beamforming). To ensure robustness in the optimization results, multiple runs were conducted for the same beam-shaping parameters but with different initial weight vectors, all of which converged to nearly identical solutions, suggesting the cost function is convex in most cases.

The genetic algorithm solver is used in MATLAB to solve (8). The solver choice is based on the complex, nonlinear nature of the cost function, which includes constraints imposed by phase-only weighting and desired beam characteristics. While gradient-based methods (e.g., Newton) are efficient for many optimization tasks, the large fluctuations in phase at the edges of the array, along with the nonlinearity of the cost function, make such methods less reliable for this synthesis problem. The genetic algorithm successfully addresses these challenges by exploring the solution space broadly. Future work could explore selective phase smoothing at the edges or gradient-based approaches if feasible within the problem’s constraints. Genetic algorithms may not strictly guarantee reaching the global optimum, but their exploratory nature

$$E(\theta, \phi) = \begin{cases} 0, & \text{if } |\theta - k\Delta\theta| \leq \theta_M \text{ and } |\phi - k\Delta\phi| \leq \phi_M \\ -\alpha(\theta - k\Delta\theta - \theta_M), & \text{if } \theta_M < |\theta - k\Delta\theta| \leq 2\theta_M \\ -\alpha(\phi - k\Delta\phi - \phi_M), & \text{if } \phi_M < |\phi - k\Delta\phi| \leq 2\phi_M \\ L, & \text{otherwise} \end{cases} \quad (10)$$

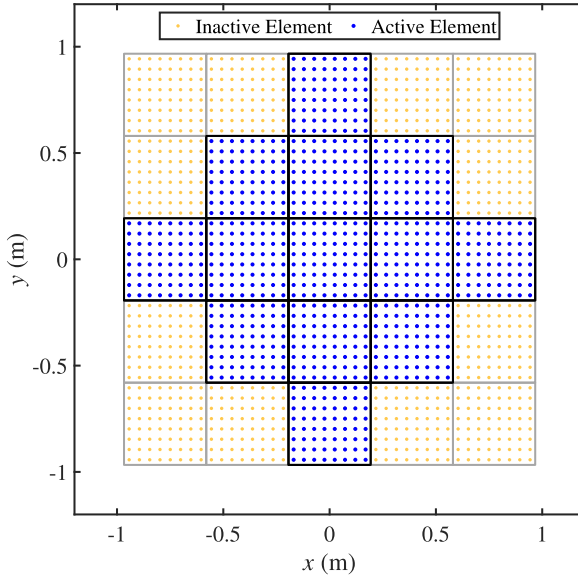


Fig. 5. Current configuration of the Horus array, with 13 active antenna panels.

TABLE I
ALGORITHM SPECIFICATIONS

Parameter	Specification
Solver	Genetic Algorithm
Objective Function	Minimize IC and EL, see eq. (8)
Envelope Function	User defined
Number of Variables	Variable (depends on control point spacing)
Selection Method	Tournament Selection
Crossover Fraction	0.75
Mutation Range (Phase)	(-180°, 180°]
Population Size	5 initial solutions
Max Generations	500 × number of variables
Max Stall Generations	10 × number of variables
Tolerance	10 ⁻⁶
Initial Population	Random (uniform phases ∈(-180°, 180°])

enables them to reliably and efficiently approach high-quality solutions.

One control point for every four antenna elements (in each dimension, x and y) is used, thus reducing the variable space by a factor of 16. The Bézier surface control points are constrained to take values from -180° to 180° . Randomization is used to initialize the set of control points. A crossover fraction of 0.75 is used with a fitness function convergence tolerance of 10^{-6} . Table I summarizes the algorithm specifications.

The focus in Section III-A and III-B will be on the synthesized transmit beams; traditional DBF methods can be applied on reception to separate the returns from the simultaneous transmit peaks. A discussion about receive beams with deterministic nulls in the directions of the transmit peaks is provided in the conclusion.

A. Peaks Offset in Azimuth or Elevation

First, we derive phase weights to produce simultaneous transmit peaks offset in either azimuth or elevation. Beam-shaping envelopes similar to those in Fig. 4(a) and (b) were used in this case. Also, since only 1-D beamforming is needed,

the Bézier surfaces are reduced to curves. Two beam patterns are produced by running the optimization twice, one with peaks spaced by 7.5° (i.e., at -7.5° , 0° , and 7.5° with respect to broadside) and the other with peaks spaced by 15° (i.e., at -15° , 0° , and 15° with respect to broadside). These are presented in Fig. 6(a) and (b).

A qualitative comparison between these patterns shows that sidelobe levels approximately 13 dB below the peaks are produced for the first case (i.e., 7.5° spacing) and of 15 dB for the second case (i.e., 15° spacing). A cut of these patterns through the elevation plane is shown in Fig. 6(d). A reduction in peak sidelobe levels as the peak spacing increases was expected since increasing the spacing allows more degrees of freedom to shape the pattern. Fig. 6(c) shows the synthesized phase weights for these beam patterns. Although the set for the beam with peaks spaced 15° shows three peaks around the center, the one for peaks spaced 7.5° does not. And while deriving a mathematical model to produce these beams without the need for a global search would be beneficial, it does not seem possible. Furthermore, rapid phase oscillations are observed near the edges of the array, which would be hard to model.

Closer peaks may be more beneficial for a scan involving a rotating PAR concept. That is, assuming the radar is mechanically rotating in azimuth and beamforming weights are applied vertically, so that simultaneous transmit peaks will be formed in elevation. Considering that traditional volume coverage patterns (VCPs) for weather surveillance only span from 0° to at most 30° , beams spaced more than 15° would not be of much use since the collected plan-position indicator (PPI) scans would span more than 30° in elevation. Ideally, simultaneous peaks at close elevation angles (e.g., every 1°) would be best since meteorological returns are spatially continuous and scans at closer elevations would be better for physical interpretation of storm dynamics. Nevertheless, the minimum spacing to achieve well-separated peaks was found empirically to be approximately $2\theta_1$, and thus, tightly packed peaks in elevation would require large apertures. It was found that as the peak spacing is set to values lower than $2\theta_1$, the peaks merge and the resulting pattern resembles that of a spoiled beam.

Another alternative is to apply the beamforming weights horizontally across the array. In this case, as the array is continuously rotating, data received from simultaneous peaks would start to overlap after the array mechanically rotates by the spacing between transmit peaks. A concept of operations for this mode was proposed in [29]. It involves a synchronized operation whereby the array mechanically rotates in azimuth and electronic steering is used in elevation to scan multiple elevations in one revolution of the antenna. That is, after the array rotates the angular spacing between simultaneous transmit peaks, all peaks are steered to the next elevation of interest. This is repeated as many times as the number of simultaneous peaks formed, to scan the same number of elevation angles. Once these sector scans at different elevations have been completed, all beams are steered back to the first elevation in the set and the process repeats. For instance, suppose three simultaneous transmit peaks where spaced by 30° , and the elevation

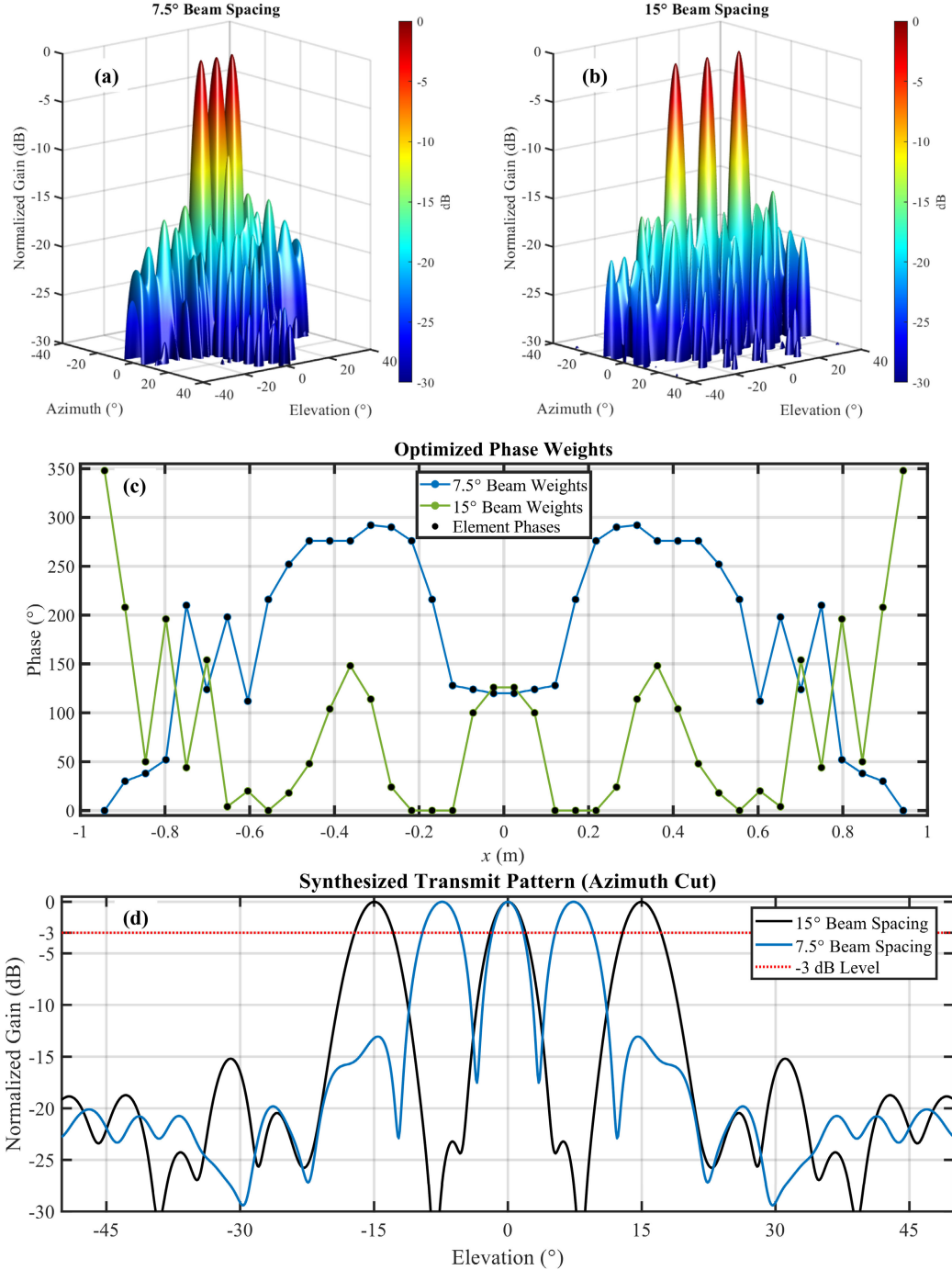


Fig. 6. Synthesized transmit antenna patterns with three simultaneous peaks in different directions, along the vertical plane (a) beams spaced by 7.5° , (b) beams spaced by 15° , (c) phase weights to generate the beams presented, and (d) cuts along the vertical principal plane. Note that transposing the phase weights produced would result in generating peaks in the horizontal plane.

angles 2° , 4° , and 6° where to be scanned. In this case, the array would first scan a 90° sector at the 2° elevation by mechanically rotating 30° . Then, all beams would be steered to 4° and another 90° sector would be collected (this time at the 4° elevation). Then, beams would be electronically steered to the 6° elevation angle and a 90° sector would be collected. Once that is completed, the transmit peaks are steered back to the first angle in the set (2° elevation) and the process repeats. After four repetitions of the process, the array has rotated

360° and three PPIs are collected at the desired elevation angles.

The described concept of operations for the transmit beams requires precise synchronization between the azimuth encoder and the beam steering controller. Furthermore, the sectors scanned for different elevation angles are collected at slightly different times, and thus, they have to be combined in post-processing. Although this would be a relatively simple step, it could produce data artifacts since precipitation systems are

constantly evolving. This would be especially important for severe weather observations (e.g., tornadic supercell storms), where storm structure can change considerably in tens of seconds.

Considering these limitations of the 1-D synthesis, 2-D antenna pattern synthesis is explored next.

B. Peaks Offset in Azimuth and Elevation

Fully digital PARs allow for 2-D antenna pattern synthesis; therefore, it is possible to synthesize beams with peaks spaced in both azimuth and elevation. Beam-shaping envelopes similar to those in Fig. 4(c) and (d) are used in this case. This is most beneficial for a couple of reasons. First, transmit peak offsets in azimuth and elevation are expected to provide better two-way sidelobe performance, which enhances the quality of polarimetric measurements. This is because receive beams formed would likely have higher sidelobe levels in the principal planes; however, the sidelobe structure on the transmit beam is more irregular and overall results in lower two-way sidelobe levels. In contrast with previous work that demonstrated only 1-D offsets [18], our method demonstrates 2-D peak offsets, which improves isolation and minimizes the impact of sidelobes. Second, this beam type allows for a simpler rotating PAR concept of operations, whereby the PAR can collect multiple continuous PPIs at different elevations with a single rotation of the array. This mitigates the need for complicated strategies as the one described in Section III-A and allows for closely spaced elevation angles to be scanned simultaneously.

A synthesized beam pattern with peaks spaced by 15° in azimuth and by 0.4° in elevation is produced to illustrate this concept, as shown in Fig. 7. In this case, the array is assumed to be mechanically tilted to the Earth-relative elevation angle of 0.9° . This set of elevation angles was chosen to match the lowest angles scanned in the Weather Surveillance Radar—1988 Doppler (WSR-88D) operational VCPs used in precipitation mode. With this transmit beam, and forming simultaneous beams on reception in the direction of the transmit peaks, PPIs are collected simultaneously at the 0.5° , 0.9° , and 1.3° elevation angles.

This beam type may be more suitable for a VCP used in a future operational network of PARs for weather surveillance. This mode supports meeting demanding requirements for the two-way peak sidelobe levels (i.e., -70 dB specified in [13]) with a smaller aperture. This is especially important at low elevation angles, where strong reflectivity gradients may be present. At higher elevations (e.g., $\geq 4^\circ$), it is unlikely to have strong reflectivity gradients that would require ultralow two-way sidelobe levels (except in cases with deep convective cores close to the radar). The main limitation is that a relatively low number of simultaneous transmit peaks can be produced (e.g., 3 or 5), which limits the achievable volume-scan time reduction. With the previous considerations, it is likely that vertically spoiled beams are more suitable at higher elevation angles. In summary, it is recommended that future VCPs for a rotating PAR should be designed using multiple simultaneous transmit beams (offset in azimuth and elevation) at low elevation angles, and vertically spoiled transmit beams at

higher elevation angles to produce high quality and temporal resolution volumes of weather observations.

IV. EXPERIMENTAL DEMONSTRATION

Beamforming weights for the transmit patterns with multiple simultaneous peaks derived using the proposed optimization are evaluated using the fully digital Horus radar. Specifically, beam types discussed in Sections III-A and III-B are implemented on transmission, and traditional DBF is used on reception to create three simultaneous beams at different steering angles. For both beam types, Horus was operated following a rotating PAR concept of operations, where the antenna is mechanically rotated clockwise in azimuth at a constant elevation angle while the array transmits and receives different beam types [12], [30].

First, the performance for both beam types discussed is evaluated using a stationary point target. Testing with known stationary ground targets provides valuable two-way measurements that demonstrate the combined performance of the transmit and receive beams, serving as a full system validation. Next, a beam with multiple transmit peak offsets in elevation is used to evaluate the performance for polarimetric weather observations. This beam type is used mainly to minimize the impact of ground clutter (since the Horus array is only ~ 4.27 m from the ground) because polarimetric weather measurements are extremely sensitive to strong ground-clutter returns.

A. Point Target

The Horus radar was deployed on June 26, 2024, in the open field located East of the Radar Innovations Laboratory (RIL), The University of Oklahoma, during a clear day with no precipitation in the area. The target of opportunity was a radio tower located in Norman, North–East of the RIL, at approximately the following coordinates: $35^{\circ}16'58.2''\text{N}$, $97^{\circ}20'19.5''\text{W}$. The tower is ~ 90 m tall and is located at a range of 14.2 km from the radar deployment site. The true azimuth angle from the radar to the tower (with respect to North) was 37.46° . Prior to conducting the experiments, the array was initialized and calibrated using the in situ mutual-coupling calibration algorithm [23], [24], [25].

Two experiments were conducted, first using a transmit beam with peaks offset only in azimuth (Section III-A), and then using a transmit beam with peaks offset in azimuth and elevation. For both experiments, the Horus antenna was tilted to 4.5° in elevation and rotated mechanically in azimuth at $12^\circ/\text{s}$. This elevation angle was selected to minimize blockage/clutter from trees in the vicinity of the radar deployment site while maintaining the beam sufficiently low to ensure it would intercept the target. A uniform pulse repetition time (PRT) of 1 ms was used, transmitting a continuous train of pulses as the antenna rotated, resulting in 30 000 pulses per revolution of the antenna ($360/12 \text{ s} \times 1000 \text{ Hz}$). Data were collected using a $30-\mu\text{s}$ nonlinearily modulated pulse compression waveform with a bandwidth of 5 MHz, centered at the transmit frequency of 3.070 MHz. The data recording period for every pulse was set to capture samples from 30 to

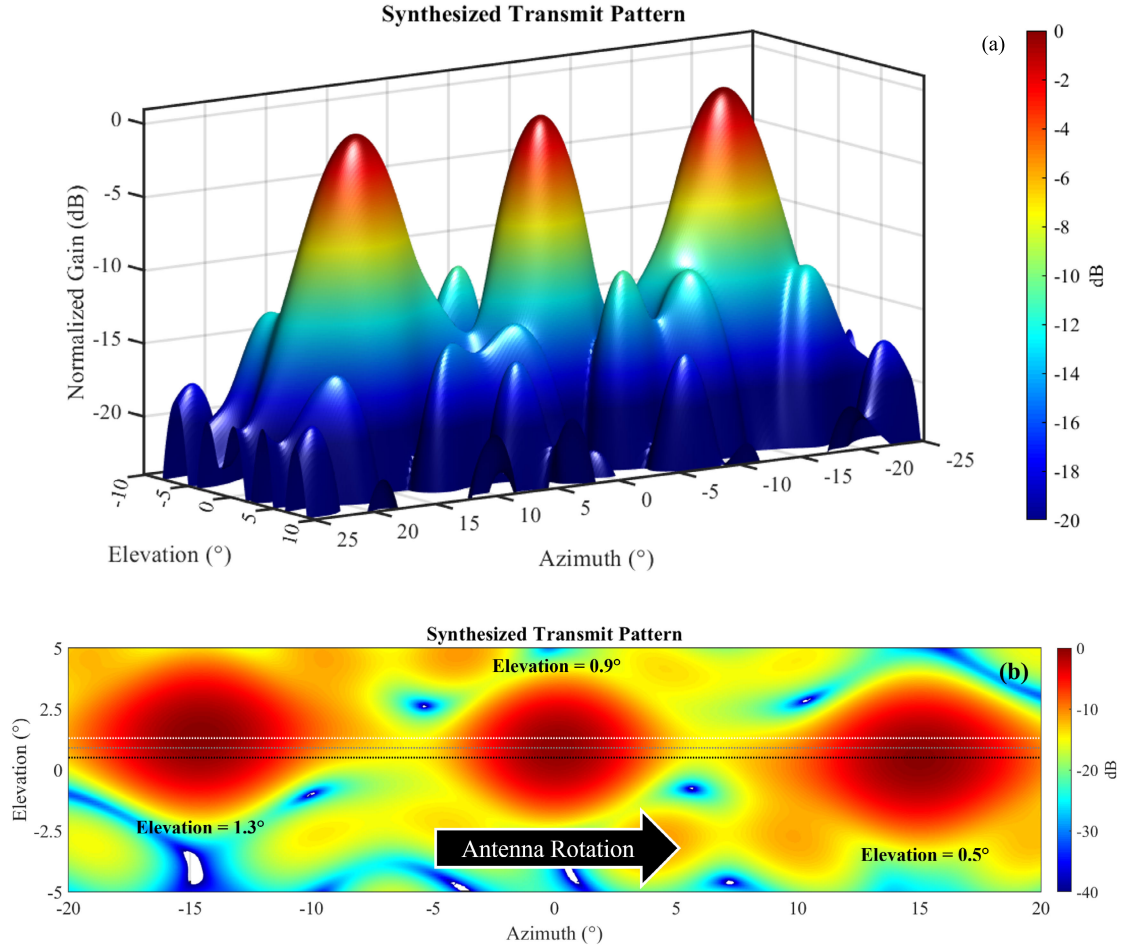


Fig. 7. Synthesized transmit antenna patterns with three simultaneous peaks spaced in by 15° in azimuth (i.e., at -15° , 0° , and 15° with respect to broadside) and by 0.4° in elevation (i.e., at -0.4° , 0° , and 0.4° with respect to broadside). Note that the array is mechanically tilted by 0.9° in elevation, so the resulting Earth-relative elevations scanned are 0.5° , 0.9° , and 1.3° : (a) 3-D view and (b) top view, where lines indicate the elevation of each beam peak.

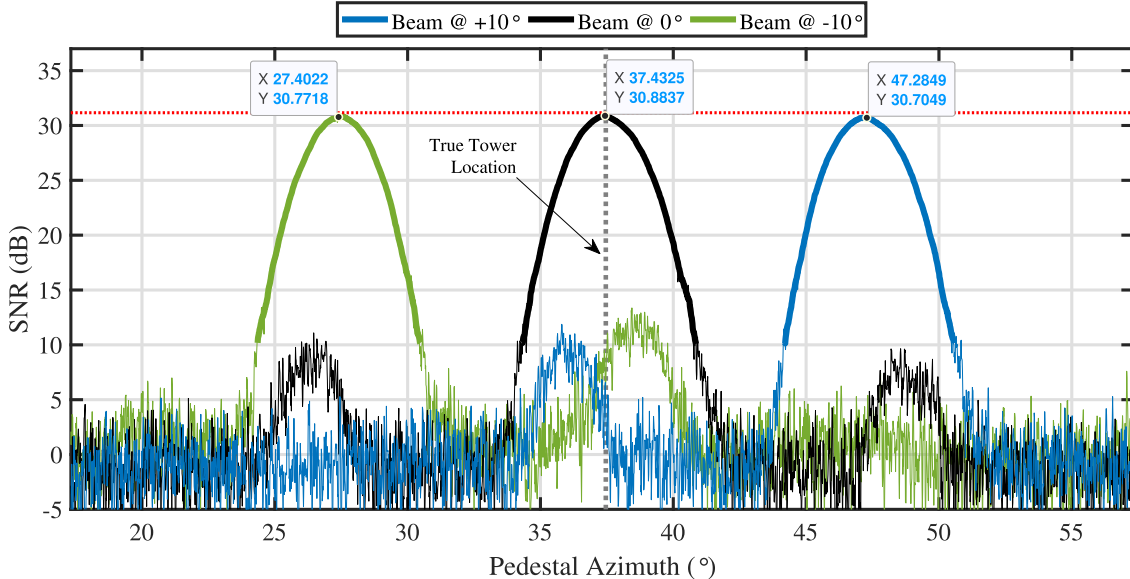


Fig. 8. Measurements from a beam with three simultaneous peaks aligned in elevation, where the abscissa shows the pedestal azimuth position (not the absolute azimuth pointing angle), and the ordinate shows the SNR. The plots show SNRs from three beams simultaneously received from the array-relative steering angles of -10° , 0° , and 10° in azimuth, and 0° in elevation.

200 μ s, which correspond to ranges between 4.5 and 30 km. Receiver range-time samples were produced at a rate of 7.8125 MHz, which results in a range sampling interval of 19.2 m.

For the first experiment, the transmit beam peaks are aligned in elevation along the horizontal principal plane and spaced by 10° in azimuth. Time-series in-phase and quadrature (IQ) data from the range with the point target were extracted for analysis. Measurements are shown in Fig. 8, where the abscissa shows the pedestal azimuth position (not the absolute azimuth pointing angle), and the ordinate shows the single-pulse signal-to-noise ratio (SNR). Pedestal azimuths are used to separate returns from the three beams (for ease of comparison) and to measure pointing offsets between different beams (which includes effects from transmit and receive). The plots show SNRs from three beams simultaneously received from the array-relative steering angles of -10° , 0° , and 10° in azimuth, and 0° in elevation. To mitigate measurement fluctuations, a running average was applied to all measurements with $\text{SNR} > 10 \text{ dB}$, with a window size of 16 pulses. Peaks are observed for each of the curves, with SNRs of approximately 31 dB. Absolute differences in peak SNRs are $\leq 0.2 \text{ dB}$, indicating that the array was well-calibrated and transmit/receive beam weights formed beams with well-aligned peaks. Angular distance between peaks is about 10.0063° between the center and leftmost beams, and 9.9124° between the rightmost and center beams. Note that the absolute azimuth angle for all peaks is approximately equal to that of the center beam, 37.41° , which is about 0.05° off from the true target location. This offset is within the expected pedestal encoder position precision and is sufficient for meteorological observations.

A qualitative evaluation indicates that all three simultaneously transmitted beams intercepted the target with relatively low clutter contamination. This is because the three plots show parabolic-like responses, resembling the mainlobe of the two-way beam patterns for each of the three peaks. This type of response is expected from an uncluttered point target. Returns from sidelobes are apparent at relatively low SNRs (i.e., $< 12 \text{ dB}$), with two sidelobe peaks for the broadside beam at about 26.5° and 48° azimuth, and one for each of the side beams at about 37° and 39° azimuth. Peak sidelobe levels observed are about -20 dB below the main beam peaks, which was expected since conventional DBF was used to form receive beams. A more effective beamforming method based on deterministic nulling will be discussed later.

The second experiment was conducted with parameters nearly identical to the first one, but this new experiment employed a transmit beam with peaks offset in azimuth and elevation. In this case, the array-relative steering angles are -15° , 0° , and 15° in azimuth, and -0.4° , 0° , and 0.4° in elevation, as in Fig. 7. Measurements are shown in Fig. 9, where three peaks are observed (as in the previous case), but with peaks spaced by approximately 15° in azimuth. Measured SNRs are approximately 31.4 dB, with absolute differences in peak SNRs $\leq 0.25 \text{ dB}$. Angular distance between peaks is about 15.044° between the center and leftmost beams, and 14.8805° between the rightmost and center beams. These are within our expected pointing precision (<a tenth of the beamwidth). Peak sidelobe levels are similar to those in the previous case although sidelobe levels in Fig. 9 appear generally higher than those in Fig. 8 along the cut presented. However, within the mainlobe of each individual two-way

beam in Fig. 9, the integrated sidelobe levels are lower compared to those in Fig. 8. This means that the increase in sidelobe levels (for the case with peaks offset in azimuth and elevation) occurs primarily outside the main transmit beam directions, reducing contamination within each mainlobe.

The quantitative results from point target measurements demonstrate the effectiveness of the proposed beamforming method, as the angular spacing and gains of the synthesized beams align with theoretical expectations. These results validate the implemented technique and its suitability for high-resolution weather radar applications.

B. Meteorological Observations

On April 27–28, 2024, a significant late-April storm system impacted OK and western north TX, USA, producing a severe weather outbreak that included at least 39 tornadoes, heavy rainfall, large hail, and damaging winds.¹ This event unfolded over a period spanning from the late morning of April 27, 2024, through the early morning of April 28, 2024. In total, 35 tornadoes were documented in OK, with 28 occurring in the National Weather Service (NWS) Norman forecast area and eight in the NWS Tulsa forecast area. The storm system also caused excessive rainfall, ranging from 4 to 8.75 in , leading to severe flash flooding and river flooding. Hail up to 3 in in diameter and severe wind gusts reaching 60 mi/h were observed during this event. These meteorological conditions provided a unique opportunity to test and validate the scan mode transmitting multiple simultaneous peaks using the fully digital Horus radar.

The Horus radar was deployed in the parking lot of The University of Oklahoma's Lloyd Noble Center (LNC) at approximately 19:30 Z (April 27, 2024). After leveling the system and positioning the array, the *in situ* mutual coupling calibration algorithm was executed. Once the array was calibrated, test scans were conducted to ensure readiness although there were no storms in the area at that time. Weather scans started around 01:02 Z (April 28, 2024) to observe a line of storms approaching from Lawton toward the Oklahoma City metropolitan area. The radar captured significant meteorological features, including heavy precipitation cores, hail cores, mesocyclones, and tornadoes, evidenced by velocity couplets and debris-like signatures observed concurrently with the KCRI radar (WSR-88D) in Norman. Adjustments were made to the radar's azimuth and elevation to track the evolving storm, including a notable tight circulation passing approximately 10 km West of Norman around 02:00 Z (April 28, 2024).

Test scans using transmit beam weights derived from the proposed technique were executed around 03:04:56 Z (April 28, 2024). The Horus antenna was positioned at 12° mechanically in elevation, and the pedestal was commanded to perform continuous rotation in azimuth at $12^\circ/\text{s}$. Simultaneous transmit beams at three elevation angles were generated, namely, 2° , 12° , and 22° . That is, transmit peaks were aligned in azimuth and offset in elevation by 10° (steering

¹Source: U.S. National Weather Service, <https://www.weather.gov/oun/events-20240427>.

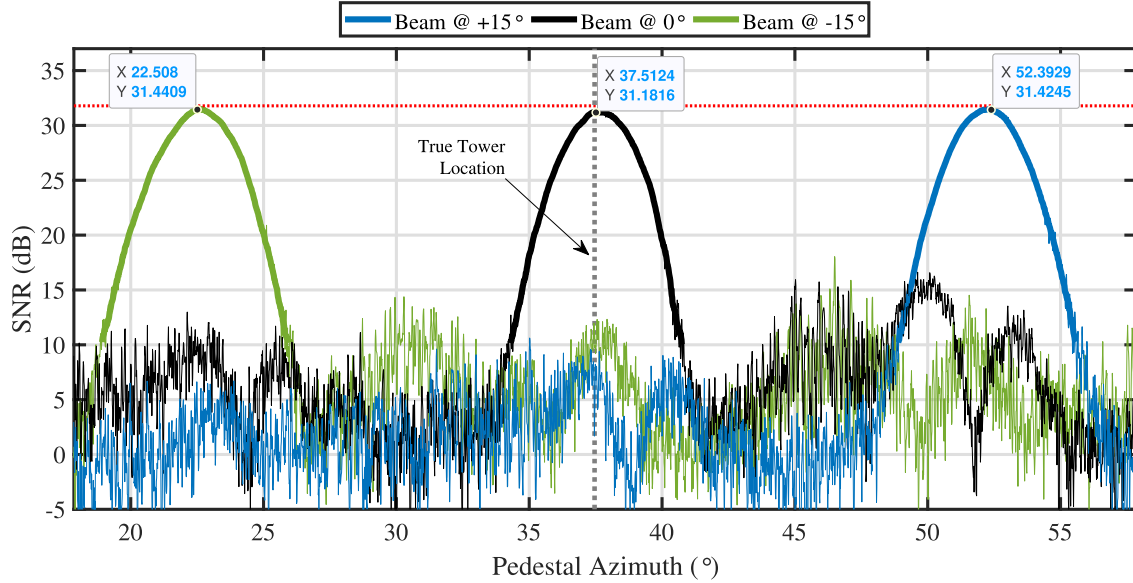


Fig. 9. Similar to Fig. 8 but for beams offset in azimuth and elevation. In this case, the array-relative steering angles are -15° , 0° , and 15° in azimuth, and -0.4° , 0° , and 0.4° in elevation.

angles of -10° , 0° , and 10°). This scan mode was chosen to reduce beam blockage (several buildings/trees around the deployment site), and collect ground-clutter-free scans at higher elevation angles. A PRT of 1 ms with 64 samples per dwell was used. Pulse compression waveforms with nonlinear frequency modulation were used, with a pulsedwidth of $80\ \mu\text{s}$ and a bandwidth of 5 MHz, resulting in a range resolution of 30 m. The progressive pulse compression technique [31], [32] was implemented to mitigate data loss during the long pulse transmission. Range-time samples were produced at a rate of 7.8125 MSPS, resulting in a range sampling interval of approximately 19.2 m. Data were collected for a range from 0.5 to 60 km for approximately 10 min, scanning the evolving storms in the vicinity of the radar.

Three simultaneous beams were formed by the real-time DBF network and time-series IQ data were recorded. Fields of polarimetric weather measurements resulting from processing the data from the scan at 03:03:45 Z (April 28, 2024) are presented in Fig. 10. The rows from top to bottom present reflectivity (Z_h), Doppler velocity (v_r), differential reflectivity (Z_{DR}), and correlation coefficient (ρ_{hv}). Columns from left to right show sets of data for each elevation angle collected simultaneously. Certain regions in the lowest elevation scan (2°) show artifacts due to beam blockage, particularly evident in the sectors to the North–East ($\sim 45^\circ$ azimuth) and to the North–West ($\sim 310^\circ$ azimuth) where abrupt changes (more apparent in ρ_{hv}) are present. This was expected since there are several buildings and trees in the near surroundings of the deployment site (parking lot of the LNC).

A qualitative evaluation of the fields indicates that data were coherently received and processed since they are relatively smooth and have realistic values. First, the Z_h field reveals a gradual shift from lower reflectivities of about 20 dBZ in the stratiform precipitation regions (North–West) to higher reflectivities up to about 60 dBZ in particular convective cores in the storm (South–East). This is consistent with expected

storm microphysics, where stronger updrafts near convective cores (i.e., regions with $Z_h > 40$ dBZ) generate a greater concentration and size of hydrometeors, thereby increasing the reflectivity. The field of v_r shows smooth variations from inbound velocities (green colors) moving toward the radar (South to North) to outbound velocities (red colors). The transition in Doppler velocity estimates going from inbound to outbound velocities through an iso-Doppler level (gray tones) indicates a smooth change in the direction of the wind field. This is typical in convective storms and represents a change in storm advection direction. Stronger shear with inbound velocities exceeding $35\ \text{m}\cdot\text{s}^{-1}$ can be seen at the mid levels (12° scan), as expected.

The fields of Z_{DR} and ρ_{hv} in Fig. 10 present relatively smooth changes with typical values. Specifically, Z_{DR} values are mostly between 0 and 4 dB and ρ_{hv} values mostly between 0.95 and 1. Z_{DR} values near 0 dB are expected at higher levels of the storm or in regions with low Z_h , indicating the presence of small nearly spherical raindrops, or randomly oriented ice particles (e.g., crystals and snow) when above the atmospheric melting layer. This is consistent with values in the PPI scans at 12° and 22° , outside of the regions with convective cores. At lower heights (or in regions with strong updrafts), Z_{DR} is larger as raindrop sizes increase, and due to air drag force, they become oblate as they fall. This increases the Z_{DR} , which explains the larger values (1–4 dB) in the lowest elevation scan (PPI at 2°).

For ρ_{hv} , most values are approximately 0.99, representing hydrometeors of the same type (e.g., raindrops and snowflakes), as expected. Accurate measurements of ρ_{hv} are crucial for polarimetric detection of the melting layer and determination of its height [33] and for identification of the areas with hail [34]. The melting layer can be seen in the PPI scans at 12° and 22° , where a circle of relatively low ρ_{hv} (~ 0.95) is present (indicated with white arrows in ρ_{hv}). Coincident with this signature, an increase in Z_h and Z_{DR}

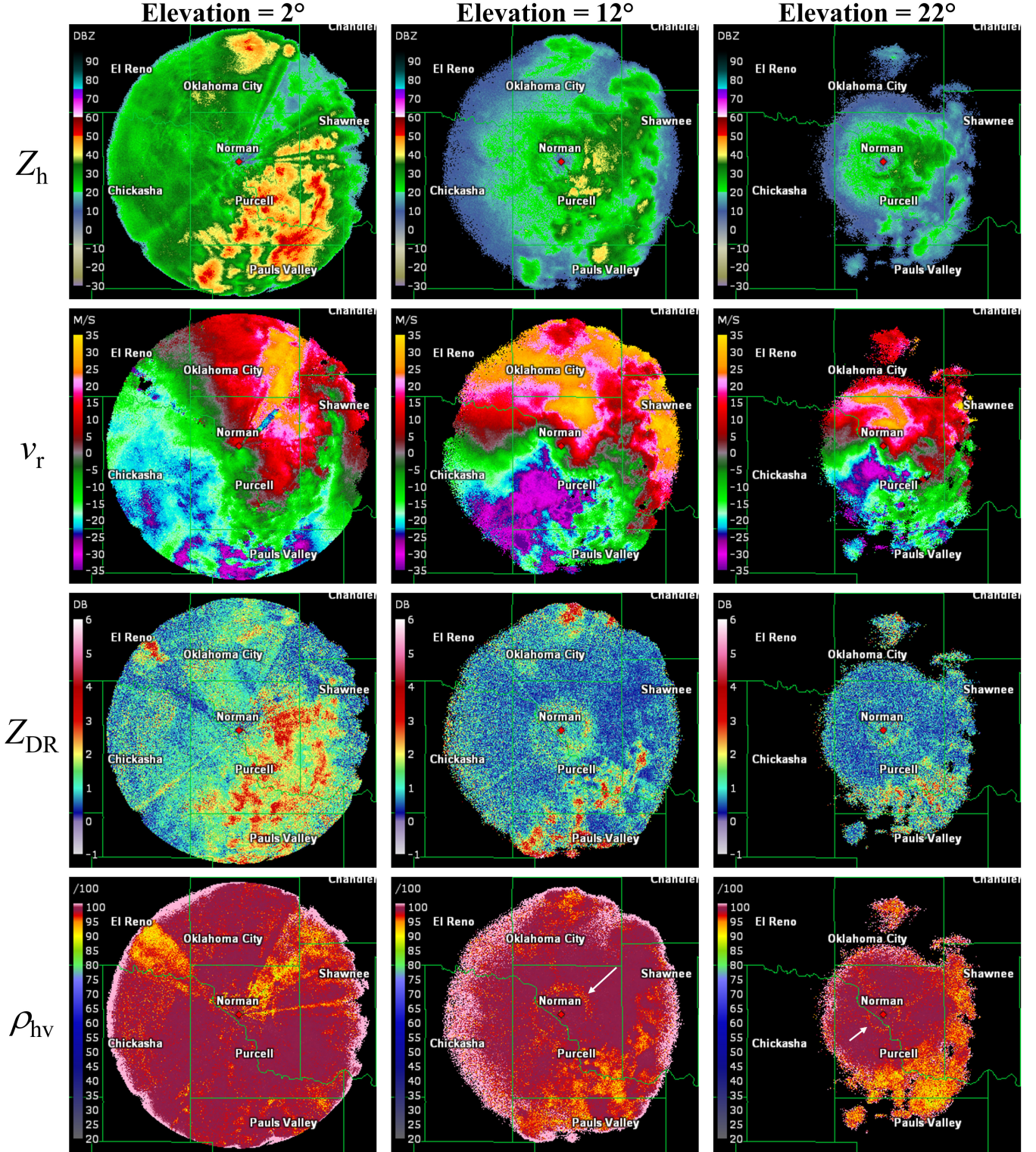


Fig. 10. Polarimetric weather observations collected simultaneously using a transmit beam with multiple peaks at 03:04:56 Z (April 28, 2024). The rows from top to bottom present reflectivity (Z_h), Doppler velocity (v_r), differential reflectivity (Z_{DR}), and correlation coefficient (ρ_{hv}). Columns from left to right show sets of data for each elevation angle collected simultaneously, 2° , 12° , and 22° elevation angles.

can be observed. Certain regions to the South–East show lower values of ρ_{hv} , coincident with storm updraft regions, where high Z_h cores are present. These may be regions where mixed-phase precipitation (i.e., raindrops and hail) is present. Lower values of ρ_{hv} (in radial directions) to the North–East

and North–West in the lowest PPI scan at 2° are attributed to beam blockage, which reduces signal powers in H and V differently, thus impacting ρ_{hv} estimates.

Data collected with Horus using the transmit mode with multiple simultaneous beams are now compared to that from

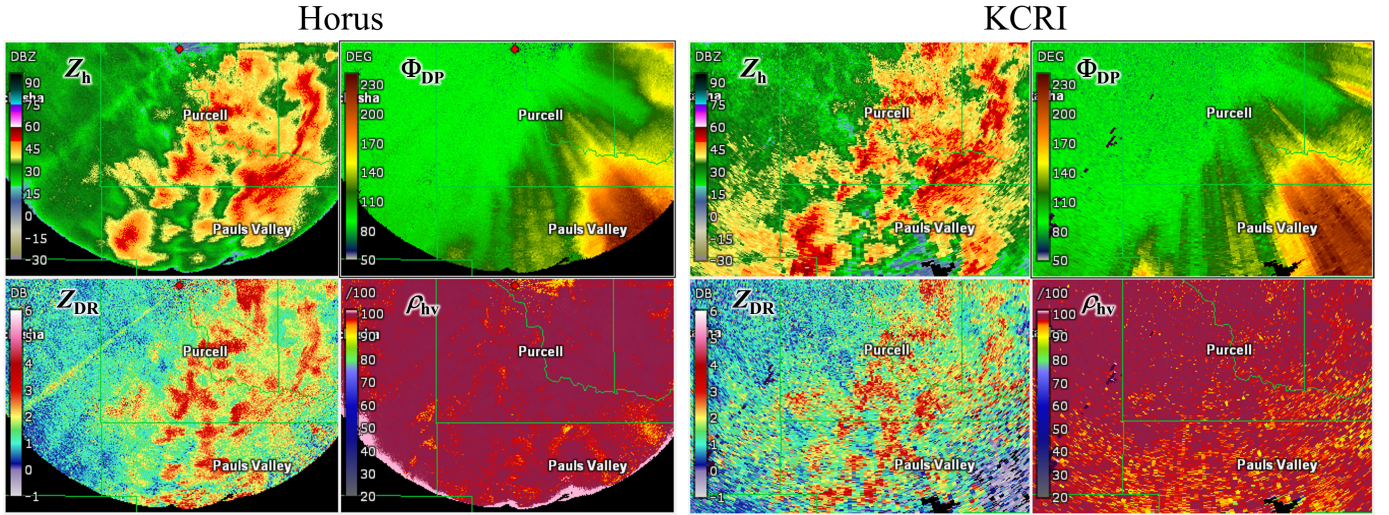


Fig. 11. Polarimetric observations from Horus 2° elevation scan 03:04:56 Z (left) and KCRI 2.5° elevation scan at 03:05:01 Z (right). Measurements from each radar include fields of Z_h , Z_{DR} , Φ_{DP} , and ρ_{hv} .

the KCRI radar, a WSR-88D in Norman, operated and maintained by the NWS radar operations center (ROC) for algorithm development, implementation, and testing. This comparison provides general validation, as the WSR-88D, a polarimetric system based on a parabolic-reflector antenna, is regularly calibrated and maintained by the ROC. Nevertheless, there are several key differences between the Horus and KCRI systems. Some of the most important differences include: radar technology (PAR versus dish-antenna), half-power beamwidth ($\sim 3^\circ$ versus $\sim 1^\circ$), sensitivity (18 dBZ at 50 km versus -7.5 dBZ at 50 km), and antenna heights (4.27 m versus 18.28 m). Despite these differences, the WSR-88D system is used as a comparison standard for Horus due to its established role in operational polarimetric weather observations and its regular calibration and maintenance. Overlapping histograms provide an effective way to compare the overall distribution of data from Horus and the WSR-88D, offering insight into how the data from a proof-of-concept radar (Horus) aligns with the operational standard despite inherent system differences. Therefore, the analysis will be mostly qualitative, focusing on statistical measurement distributions using histograms.

Data from the lowest elevation scan collected with Horus are used since most significant polarimetric signatures are present at lower altitudes. Data are shown in Fig. 11, where the left panels correspond to Horus and the right ones to KCRI. In this case, radar measurements similar to those in Fig. 10 are shown, except that v_r was replaced by differential phase (Φ_{DP}). This is to illustrate all polarimetric variables and because v_r is more challenging to compare as it depends on radar location and the systems were not collocated during this experiment. A qualitative comparison between corresponding panels shows that similar storm features are observed, despite system differences described. As expected, the coarser Horus beamwidth smears some storm features in the angular dimension compared to KCRI (beamwidth of 3° versus 1°). Estimates from Horus seem to be unbiased compared to those from KCRI, as the

overall mean values are similar. A lower standard deviation of estimates is apparent in Horus measurements. This is likely due to the higher number of samples integrated in processing (i.e., longer dwell time), compared to those used in KCRI. Nevertheless, the goal of this analysis is to compare meteorological features and broad statistical similarity.

To further assess the performance of the proposed beam-forming method, bivariate density maps comparing polarimetric variable estimates from the Horus radar and the KCRI radar were produced. Data with $SNR > 10$ dB were extracted to ensure high data quality, and from the lower half of the scan in Fig. 11 (i.e., azimuth angles from 90° to 270°), to minimize impacts from beam blockage. These density maps are normalized to approximate a probability density function, that is, the value at each bin is computed as the number of observations in that bin divided by the product of the total number of observations and the area of the bin. The Pearson correlation coefficient r between the estimates is indicated in each subfigure title. The resulting scatterplots are presented in Fig. 12.

Results indicates a significant correlation (i.e., $r > 0.9$) for estimates in Fig. 12(a) Z_h , and Fig. 12(b) Φ_{DP} . Results in Fig. 12(c) Z_{DR} and Fig. 12(d) ρ_{hv} also show considerable correlation ($r \geq 0.8$) between these polarimetric estimates, which are typically very sensitive to noise and estimation error [34]. It is important to note that the bivariate maps are approximately symmetric about the $x = y$ line, and most of the estimates lie on or very close to this line. This indicates that estimates from the Horus scan with multiple simultaneous beams are not biased, and that measurement errors may be larger for these polarimetric variables. These results are consistent with those presented in [30], where polarimetric data from a PAR (the NOAA/NSSL Advanced Technology Demonstrator) and a prototype WSR-88D (KOUN) were quantitatively compared.

Despite the encouraging results, it is essential to emphasize that these comparisons are subject to inherent limitations due

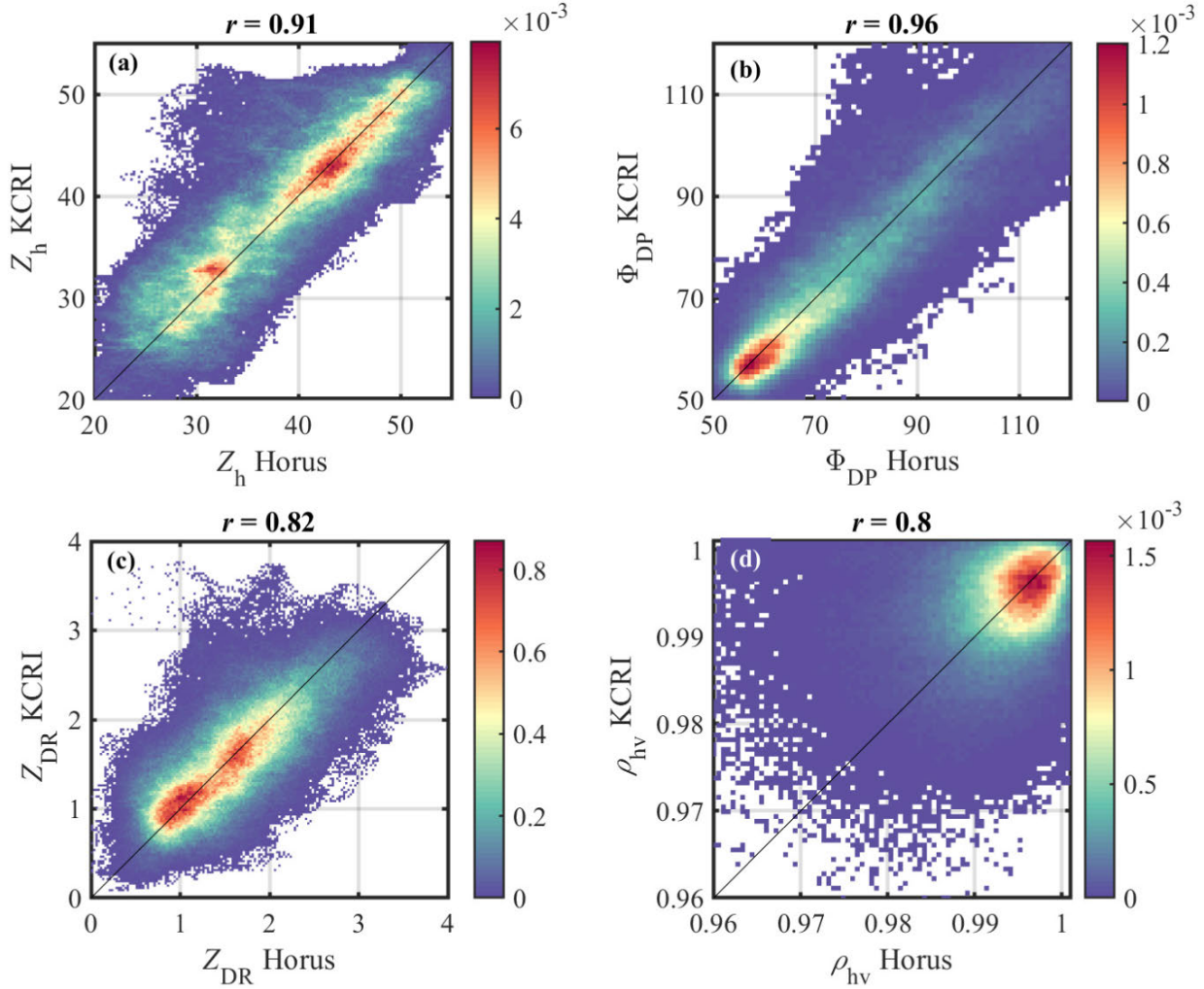


Fig. 12. Bivariate density maps of (a) Z_h , (b) Φ_{DP} , (c) Z_{DR} , and (d) ρ_{hv} , using data (with SNR > 10 dB) from both systems under consideration. These density maps are normalized to approximate a probability density function (i.e., unit area). The Pearson correlation coefficient r between the estimates is indicated in each subfigure title.

TABLE II
POLARIMETRIC DATA STATISTICAL COMPARISON

Horus		KCRI		
Mean	Standard Deviation	Mean	Standard Deviation	
Z_h (dBZ)	41.4172	1.7384	40.9575	1.8161
Z_{DR} (dB)	1.7918	0.1049	1.7967	0.0939
Φ_{DP} ($^{\circ}$)	109.9329	9.2317	109.3556	8.3391
ρ_{hv} (\sim)	0.9935	0.0013	0.9914	0.0048

to differences in system parameters, such as beamwidth, range resolution, and data collection strategies. Moreover, the radars were not colocated, and the data were collected independently, introducing some spatial and temporal discrepancies. A more controlled and coordinated experiment, with synchronized data collection and colocated radars, could further reduce biases and provide a more robust evaluation of the proposed technique. Future work will aim to conduct such experiments

to enable more precise, quantitative validation of the beam-forming method.

A summary of the statistical characteristics extracted from the bivariate density maps is presented in Table II. It can be seen that the corresponding means and standard deviations of Horus and KCRI data are in good agreement.

V. CONCLUSION

In this article, an algorithm to design phase-only beam-forming weights to produce beams with multiple simultaneous peaks was presented, and its efficacy was demonstrated using the fully digital Horus radar. This beamforming technique enables the generation of multiple simultaneous transmit beams, which can enhance temporal resolution by a factor proportional to the number of peaks. The primary motivation for this work is the need for high-temporal-resolution weather measurements, essential for the next-generation weather surveillance. Compared to traditional spoiled beams, the multiple simultaneous peaks approach offers distinct advantages. It reduces two-way sidelobe levels, which is crucial for

minimizing contamination from strong reflectivity gradients—particularly valuable in severe weather scenarios where high reflectivity cores can contaminate measurements. Furthermore, maintaining low sidelobe levels is essential for the integrity of polarimetric measurements, which support the differentiation of hydrometeors and enhance quantitative precipitation estimation. Additionally, the ability to generate multiple simultaneous beams allows for more flexible and efficient scanning strategies that can dynamically adapt to fast-evolving weather. High-quality polarimetric data, combined with rapid update rates, enables meteorologists to better identify and track severe weather phenomena such as thunderstorms, tornadoes, and hurricanes, ultimately providing more timely and accurate warnings.

The contributions of this work are: 1) introducing a phase-only beamforming technique that synthesizes multiple simultaneous transmit beams; 2) synthesizing beams with peaks offset in both azimuth and elevation, for more effective sidelobe mitigation; and 3) demonstrating the method through actual deployments with the fully digital Horus PAR. These contributions present a significant advancement in PAR technology for weather applications, achieving high data quality and rapid temporal resolution within the practical constraints of operational systems.

The optimization algorithm developed in this study effectively generated phase-only weights for beamforming, resulting in improved sensitivity (due to the absence of amplitude tapering), superior sidelobe isolation, and well-defined two-way patterns. While some two-way sidelobes remained relatively high, this was attributed to the straightforward implementation of beamforming weights on reception discussed in this article (e.g., Fourier beamforming). To further reduce unwanted returns, precomputed weights can be applied to the digital receive channels, minimizing the array response at the angles of interfering transmit beams. Deterministic nulls can be placed in directions coinciding with two out of the three transmit beam peaks at a time. If the array is well-calibrated, these nulls can be extremely deep, lowering the two-way response below -60 dB at the angles of the interfering transmit beams. However, the presence of randomly failed transmit-receive elements and calibration errors can significantly reduce the effectiveness of the nulling unless the locations of the failed elements are known and accounted for when determining the appropriate weights. Demonstrating the placement of deterministic nulls on reception, coupled with multiple beams on transmission is the next step in our research. Furthermore, it is noted that performance characteristics—such as sidelobe levels and synthesis convergence time—are influenced by the algorithm's parameters and configuration. A more comprehensive investigation into these dependencies is planned for future work.

Experimental validation was conducted through point target tests and weather observations during the severe weather event on April 27-28, 2024. The point target tests demonstrated that the Horus radar, using the multiple simultaneous peaks beamforming technique, achieved precise and consistent beam pointing. Measurements from a radio tower located 14.2 km from the radar showed SNRs of approximately

31 dB, with absolute differences in peak SNRs ≤ 0.2 dB. Angular distances between peaks were 10.0063° and 9.9124° , indicating well-aligned beams and effective calibration. These results validate the combined performance of the transmit and receive beams, confirming the effectiveness of the beamforming weights derived from the optimization algorithm.

The weather demonstration provided further validation, capturing significant meteorological features in heavy precipitation cores. Qualitative comparisons presented in Section IV-B highlight the smooth and coherent depiction of storm structures by the Horus radar. Features such as heavy precipitation cores, reflectivity gradients, and polarimetric fields align closely with those observed by the KCRI radar (WSR-88D), underscoring the effectiveness of the proposed technique. Scatterplots comparing data from the Horus radar with the KCRI WSR-88D radar showed considerably high correlations for key polarimetric variables, including reflectivity (Z_h , $r = 0.91$), differential reflectivity (Z_{DR} , $r = 0.82$), differential phase (Φ_{DP} , $r = 0.96$), and correlation coefficient (ρ_{hv} , $r = 0.80$). These results confirm that the Horus radar produces high-quality polarimetric measurements comparable to an operational weather radar. However, it is important to note that the comparison is subject to limitations due to differences in system parameters and data collection strategies. A more controlled, coordinated experiment between the radars could provide an even stronger quantitative evaluation of the proposed method.

The findings from this article illustrate the potential of the beam with multiple simultaneous peaks for advanced weather surveillance. This method provides significant advantages in terms of improving temporal resolution and maintaining high data quality, making it an attractive candidate for the next-generation weather radar systems. Future work will investigate deterministic nulling methods for DBF on reception and evaluate their performance under a wider range of meteorological conditions.

ACKNOWLEDGMENT

The authors express their appreciation to Dr. Booneng Cheong (OU ARRC), who designed the conceptual illustration of the beam patterns (Fig. 1) in this article. The views, opinions, and/or findings contained in this article are those of the author(s) and should not be construed as an official U.S. Government position, policy, or decision, unless so designated by other documentation.

REFERENCES

- [1] A. Ryzhkov and D. Zrnic, *Radar Polarimetry for Weather Observations*. Berlin, Germany: Springer, 2019. [Online]. Available: <https://books.google.com/books?id=d0uYvQEACAAJ>
- [2] D. J. Stensrud et al., “Convective-scale warn-on-forecast system: A vision for 2020,” *Bull. Amer. Meteorological Soc.*, vol. 90, no. 10, pp. 1487–1500, Oct. 2009. [Online]. Available: https://journals.ametsoc.org/view/journals/bams/90/10/2009bams2795_1.xml
- [3] M. Weber et al., “Towards the next generation operational meteorological radar,” *Bull. Amer. Meteorological Soc.*, vol. 102, no. 7, pp. 1357–1383, Jul. 2021.
- [4] D. S. Zrnic et al., “Agile-beam phased array radar for weather observations,” *Bull. Amer. Meteorolog. Soc.*, vol. 88, no. 11, pp. 1753–1766, Nov. 2007, doi: [10.1175/BAMS-88-11-1753](https://doi.org/10.1175/BAMS-88-11-1753).

- [5] R. D. Palmer et al., "A primer on phased array radar technology for the atmospheric sciences," *Bull. Amer. Meteorological Soc.*, vol. 103, no. 10, pp. 2391–2416, Jul. 2022. [Online]. Available: <https://journals.ametsoc.org/view/journals/bams/103/10/BAMS-D-21-0172.1.xml>
- [6] P. L. Heinselman, D. L. Priegnitz, K. L. Manross, T. M. Smith, and R. W. Adams, "Rapid sampling of severe storms by the national weather radar tested phased array radar," *Weather Forecasting*, vol. 23, no. 5, pp. 808–824, Oct. 2008. [Online]. Available: https://journals.ametsoc.org/view/journals/wefo/23/5/2008waf2007071_1.xml
- [7] K. A. Bowden, P. L. Heinselman, D. M. Kingsfield, and R. P. Thomas, "Impacts of phased-array radar data on forecaster performance during severe hail and wind events," *Weather Forecasting*, vol. 30, no. 2, pp. 389–404, Apr. 2015. [Online]. Available: https://journals.ametsoc.org/view/journals/wefo/30/2/waf-d-14-00101_1.xml
- [8] J. E. Stailey and K. D. Hondl, "Multifunction phased array radar for aircraft and weather surveillance," *Proc. IEEE*, vol. 104, no. 3, pp. 649–659, Mar. 2016.
- [9] B. Isom et al., "The atmospheric imaging radar: Simultaneous volumetric observations using a phased array weather radar," *J. Atmos. Ocean. Technol.*, vol. 30, no. 4, pp. 655–675, Apr. 2013.
- [10] J. M. Kurdzo et al., "Observations of severe local storms and tornadoes with the atmospheric imaging radar," *Bull. Amer. Meteorolog. Soc.*, vol. 98, no. 5, pp. 915–935, May 2017. [Online]. Available: <https://journals.ametsoc.org/view/journals/bams/98/5/bams-d-15-00266.1.xml>
- [11] F. Mizutani et al., "Fast-scanning phased-array weather radar with angular imaging technique," *IEEE Trans. Geosci. Remote Sens.*, vol. 56, no. 5, pp. 2664–2673, May 2018.
- [12] D. Schwartzman, S. M. Torres, and T. Yu, "Distributed beams: Concept of operations for polarimetric rotating phased array radar," *IEEE Trans. Geosci. Remote Sens.*, vol. 59, no. 11, pp. 9173–9191, Nov. 2021.
- [13] NOAA/NWS. (2015). *Radar Functional Requirements*. [Online]. Available: https://roc.noaa.gov/WSR88D/PublicDocs/NOAA_Radar_Functional_Requirements_Final_Sept%202015.pdf
- [14] D. S. Zrnic, V. M. Melnikov, R. J. Doviak, and R. Palmer, "Scanning strategy for the multifunction phased-array radar to satisfy aviation and meteorological needs," *IEEE Geosci. Remote Sens. Lett.*, vol. 12, no. 6, pp. 1204–1208, Jun. 2015.
- [15] V. M. Melnikov, R. J. Doviak, and D. S. Zrnic, "A method to increase the scanning rate of phased-array weather radar," *IEEE Trans. Geosci. Remote Sens.*, vol. 53, no. 10, pp. 5634–5643, Oct. 2015.
- [16] D. Schwartzman, R. D. Palmer, M. Herndon, and M. Yeary, "Pattern synthesis and digital beamforming capabilities of the fully digital Horus radar," in *Proc. IEEE Radar Conf.*, May 2024, pp. 1–6.
- [17] K. Hondl and M. Weber, "NOAA's meteorological phased array radar research program," in *Proc. IEEE Int. Symp. Phased Array Syst. Technol. (PAST)*, Oct. 2019, pp. 1–6.
- [18] E. Yoshikawa, T. Ushio, and H. Kikuchi, "A study of comb beam transmission on phased array weather radars," *IEEE Trans. Geosci. Remote Sens.*, vol. 59, no. 8, pp. 6346–6356, Aug. 2021.
- [19] G. C. Brown, J. C. Kerce, and M. A. Mitchell, "Extreme beam broadening using phase only pattern synthesis," in *Proc. IEEE Workshop Sensor Array Multichannel Signal Process.*, Jul. 2006, pp. 36–39.
- [20] D. P. Scholnik, "A parameterized pattern-error objective for large-scale phase-only array pattern design," *IEEE Trans. Antennas Propag.*, vol. 64, no. 1, pp. 89–98, Jan. 2016.
- [21] D. Schwartzman, R. Palmer, T.-Y. Yu, R. Reinke, and F. Nai, "A pattern synthesis method for polarimetric weather observations with the all-digital Horus phased array radar," in *Proc. 102nd Amer. Meteorological Soc. Annu. Meeting*, 2022. [Online]. Available: https://ams.confex.com/ams/102ANNUAL/mediafile/Handout/Paper395979/AMS_2022_PatternSynthesis.pdf
- [22] R. J. Reinke, D. Schwartzman, F. Nai, T. Yu, J. Salazar-Cerreño, and R. D. Palmer, "Evaluation of a spline-based parameterization scheme for phase-only antenna pattern synthesis," in *Proc. IEEE Int. Symp. Phased Array Syst. Technol. (PAST)*, Oct. 2022, pp. 1–8.
- [23] R. D. Palmer et al., "Horus—A fully digital polarimetric phased array radar for next-generation weather observations," *IEEE Trans. Radar Syst.*, vol. 1, pp. 96–117, 2023.
- [24] C. Fulton et al., "Mutual coupling-based calibration for the Horus digital phased array radar," in *Proc. IEEE Int. Symp. Phased Array Syst. Technol. (PAST)*, Oct. 2022, pp. 1–6.
- [25] M. Herndon, D. Schwartzman, C. Fulton, and M. Yeary, "Self-calibration of the Horus all-digital phased array using mutual coupling," in *Proc. IEEE Radar Conf.*, May 2024, pp. 1–6.
- [26] A. V. Ryzhkov, S. E. Giangrande, V. M. Melnikov, and T. J. Schuur, "Calibration issues of dual-polarization radar measurements," *J. Atmos. Ocean. Technol.*, vol. 22, no. 8, pp. 1138–1155, Aug. 2005. [Online]. Available: https://journals.ametsoc.org/view/journals/atot/22/8/jtech1772_1.xml
- [27] R. J. Doviak and D. Zrnic, *Doppler Radar and Weather Observations*. Mineola, NY, USA: Dover, 2006.
- [28] G. Buttazzoni and R. Vescovo, "Power synthesis for reconfigurable arrays by phase-only control with simultaneous dynamic range ratio and near-field reduction," *IEEE Trans. Antennas Propag.*, vol. 60, no. 2, pp. 1161–1165, Feb. 2012.
- [29] D. Schwartzman, M. Weber, S. Torres, H. Thomas, D. S. Zrnic, and I. Ivic, "Scanning concepts and architectures supporting rotating meteorological phased-array radar," in *Proc. 101st Amer. Meteorological Soc. Annu. Meeting*, 2021.
- [30] D. Schwartzman, "Signal processing techniques and concept of operations for polarimetric rotating phased array radar," Ph.D. dissertation, Dept. Elect. Comput. Eng. (ECE), Univ. Oklahoma, Norman, OK, USA, 2020. [Online]. Available: <https://hdl.handle.net/11244/326580>
- [31] C. M. Salazar Aquino, B. Cheong, and R. D. Palmer, "Progressive pulse compression: A novel technique for blind range recovery for solid-state radars," *J. Atmos. Ocean. Technol.*, vol. 38, no. 9, pp. 1599–1611, Jul. 2021. [Online]. Available: <https://journals.ametsoc.org/view/journals/atot/38/9/JTECH-D-20-0164.1.xml>
- [32] C. M. Salazar, B. Cheong, R. D. Palmer, D. Schwartzman, and A. V. Ryzhkov, "Improvements in the compression filter and calibration factor of the progressive pulse compression technique," *IEEE Trans. Geosci. Remote Sens.*, vol. 62, 2024, Art. no. 5101814.
- [33] A. Ryzhkov and J. Krause, "New polarimetric radar algorithm for melting-layer detection and determination of its height," *J. Atmos. Ocean. Technol.*, vol. 39, no. 5, pp. 529–543, May 2022. [Online]. Available: <https://journals.ametsoc.org/view/journals/atot/aop/JTECH-D-21-0130.1/JTECH-D-21-0130.1.xml>
- [34] D. S. Zrnic and A. V. Ryzhkov, "Polarimetry for weather surveillance radars," *Bull. Amer. Meteorolog. Soc.*, vol. 80, no. 3, pp. 389–406, Mar. 1999, doi: [10.1175/1520-0477\(1999\)080<0389:PFWSR>2.0.CO;2](https://doi.org/10.1175/1520-0477(1999)080<0389:PFWSR>2.0.CO;2).



David Schwartzman (Senior Member, IEEE) was born in Piracicaba, Brazil, in 1988. He received the M.S. and Ph.D. degrees in electrical and computer engineering from The University of Oklahoma (OU), Norman, OK, USA, in 2015 and 2020, respectively, with a focus on polarimetric phased array radar.

He has held research positions supporting the NOAA National Severe Storms Laboratory (NSSL) and the Advanced Radar Research Center (ARRC), OU. At NSSL, he gained key insights into observational needs for improving weather warnings and forecasts and developed signal processing algorithms to enhance meteorological products for the operational U.S. Weather Surveillance Radar (WSR-88D). He is currently an Assistant Professor with a joint appointment with the School of Meteorology and the School of Electrical and Computer Engineering, OU, affiliated with the ARRC. His work spans signal and array processing, radar calibration, and the development of advanced radar techniques for weather observation and severe weather detection.

Dr. Schwartzman has received awards including the 2024 Research Excellence Award from the College of Atmospheric and Geographic Sciences, OU, the 2023 IEEE Region 5 Outstanding Young Professional Award, and the 2019 American Meteorological Society (AMS) Spiros G. Geotis Prize. He is an Active Member of AMS, where he contributes to its Scientific and Technological Activities Commission (STAC) on Radar Meteorology. He serves as a Topical Associate Editor for IEEE TRANSACTIONS ON GEOSCIENCE AND REMOTE SENSING (TGRS).



Robert D. Palmer (Fellow, IEEE) was born in Fort Moore (formerly Fort Benning), GA, USA, in 1962. He received the Ph.D. degree in electrical engineering from The University of Oklahoma (OU), Norman, OK, USA, in 1989.

From 1989 to 1991, he was a JSPS Post-Doctoral Fellow with the Radio Atmospheric Science Center, Kyoto University, Kyoto, Japan, where his major accomplishment was the development of novel interferometric radar techniques for studies of atmospheric turbulent layers. After his stay in Japan, he was with the Physics and Astronomy Department, Clemson University, Clemson, SC, USA. From 1993 to 2004, he was a Faculty Member with the Department of Electrical Engineering, University of Nebraska, Lincoln, NE, USA, where his interests broadened into areas including wireless communications, remote sensing, and pedagogy. Soon after moving to OU as the Tommy C. Craighead Chair of the School of Meteorology in 2004, he established the interdisciplinary Advanced Radar Research Center (ARRC). He currently serves as the Executive Director of ARRC and OU's Associate Vice-President of research and partnerships. While at OU, his research interests have focused on the application of advanced radar signal processing techniques to observations of severe weather, particularly related to phased array radars and other innovative system designs. He has authored widely in the area of radar sensing of the atmosphere, with over 130 peer-reviewed journal articles, one textbook, 50 international invited talks, and hundreds of conference presentations.

Prof. Palmer is a fellow of the American Meteorological Society (AMS) emphasizing his dedication to the interdisciplinary nature of radar science.



Mark B. Yeary (Fellow, IEEE) received the Ph.D. degree from the Department of Electrical Engineering, Texas A&M University, College Station, TX, USA, in 1999.

Since the fall of 2002, he has been with the School of Electrical and Computer Engineering, The University of Oklahoma (OU), Norman, OK, USA, where he was named the Endowed Hudson-Torchmark Presidential Professor in 2011. In 2022, he was awarded OU's George Lynn Cross Research Professorship and named the Gallogly Chair Professorship within OU's Gallogly College of Engineering. Since 2005, he has been a Founding Member of the Advanced Radar Research Center (ARRC), OU, which is now the largest university-based radar center in the nation. For instance, he was deeply involved in the National Weather Radar Testbed, the ARRC's Atmospheric Imaging Radar Program, and the ARRC's Horus Program. His research interests are in the areas of digital signal processing and radar systems with an emphasis on hardware prototype development.

Dr. Yeary is a licensed Professional Engineer. He is also a fellow of the Cooperative Institute for Severe and High-Impact Weather Research and Operations (CIWRO), National Weather Center, Norman. He served as a Co-Chair for the 2018 IEEE Radar Conference in Oklahoma City, and he has been serving as a Chair for the Radar Sessions at the American Meteorological Society (AMS) Annual Meetings since 2009. He serves as a Faculty Advisor for OU's American Indians in Science and Engineering Society (AISES) Chapter. He has served as a PI or a Co-PI for grants from ONR, NASA, NSF, NOAA, and DARPA.



Matthew Herndon (Member, IEEE) received the B.S. degree (magna cum laude) in computer engineering and the M.S. degree in electrical and computer engineering from The University of Oklahoma (OU), Norman, OK, USA, in 2017 and 2022, respectively.

He joined the Advanced Radar Research Center (ARRC), OU, in 2017, and has contributed to a variety of projects as a Full-Time Radar Engineer and a Part-Time Graduate Student. He specializes in software system design/integration, data visualization, and phased array radar.

Mr. Herndon received the ARRC Journal Paper Award in 2021.